MB adsorption by TiO_2/GO nanocomposites: A comparison of the synthesis method

Francisco J. Cano
Nanociencias y Nanotecnología, CINVESTAV, México
IMMM, Le Mans Université, France
franciscojavier.cano@cinvestav.edu.mx
francisco.gomez_cano.etu@univ-lemans.fr

O. Reyes-Vallejo
Ingeniería eléctrica (SEES), CINVESTAV- IPN, México
odin.reyes.v@cinvestav.mx

Araceli Romero-Núñez
Ingeniería eléctrica (SEES), CINVESTAV- IPN, México
araceli.romero@cinvestav.mx

Javier Covarrubias García
Ingeniería eléctrica (SEES), CINVESTAV- IPN, México
javier.covarrubias.g@cinvestav.mx

A. García-Sotelo
Departamento de Física, CINVESTAV- IPN, México
alex@fis.cinvestav.mx

S. Velumani
Ingeniería eléctrica (SEES), CINVESTAV- IPN, México
velu@cinvestav.mx

A. Kassiba
IMMM, Le Mans Université, France
abdelhadi.kassiba@univ-lemans.fr

Abstract— *Graphene oxide (GO) was synthesized by the Tour method and incorporated into a commercial anatase TiO_2 matrix by photo-sonication and ball-milling methods, respectively. By XRD, Raman, and FT-IR we checked the oxidation of graphite to GO and compared the characteristics of TiO_2/GO nanocomposites obtained by both methods. Finally, we evaluated the percentage removal by adsorption of Methylene blue (MB). For commercial TiO_2, results exhibit a maximum removal of ~33.9% after 210 min of exposure. Likewise, after incorporation of GO to TiO_2, the removal increased to ~40.57% in materials synthesized by the photo-sonication method, while by the ball-milling method the maximum removal percentage was ~65.11%. So that with this work we propose ball-milling as the most suitable method for the fabrication of TiO_2/GO nanocomposites for application in MB removal by the adsorption mechanism.*

Keywords: TiO_2, graphene oxide, nanocomposites, methylene blue

1. Introduction

Titanium dioxide is one of the most promising modern materials [1]. However, the use of pure TiO_2 nanoparticles is hampered by some limitations such as low adsorption capacity, thus reducing its efficiency for wastewater and natural water-body purification processes of organic pollutants. To overcome such limitations, several strategies have been developed to improve the efficiency of the material without the use of additional energy sources, for example, implantation of metal ions [2-4], synthesis of reduced photocatalyst TiO_2 with nonmetals [5, 6], morphological modification [7], modification with rare earth compounds [8, 9], as well as the formation of TiO_2 composites with other materials [10, 11], which have recently taken great interest due to the considerable improvement of the material properties.

Due to their unusual structural and electronic properties [14] and their high adsorption capacity [15], graphene oxides can be used to enhance the sorption properties of TiO_2 when preparing nanocomposites [12, 13]. Different methods have been reported for the design of the latter, some examples are hydrothermal synthesis [16], sol-gel [17], sputtering [18], and ball-milling [19]. The structural characteristics, and therefore the sorption properties, will depend largely on the synthesis route, thus opening the possibility of designing materials according to specific needs.

In this work, we synthesized graphene oxide (GO) by the Tour method and subsequently incorporated it into a commercial TiO_2 matrix (*particle size < 25 nm*) by photo-sonication and ball milling, using a TiO_2: GO weight ratio of 98:2. The obtained nanocomposites were characterized by X-Ray Diffraction (XRD), Raman spectroscopy, Fourier Transform Infrared spectroscopy (FT-IR). Finally, the adsorption removal efficiency of methylene blue (MB) was compared with each nanocomposite synthesized by both methods.

2. Experimental procedure

2.1. Graphene oxide by Tour method

The graphene oxide (GO) synthesis by the Tour method [20] was carried out by combining 43.2 mL of concentrated H_2SO_4 (sulfuric acid ACS reagent, 95.0-98.0%) with 4.8 mL of concentrated H_3PO_4 (orthophosphoric acid, 85%) in a ratio of 9:1(v/v). Next, 1 g of graphite powder was added to the acid mixture and kept under constant stirring for 3 hours and then 3 g of $KMnO_4$ was added. After 2 hours, a mixture of 12 mL of analytical grade H_2O_2 (30% w/w) and 13 mL of HCl (36.5%-38.0%) was added dropwise. After 30 min, distilled water was added to the mixture to stop the reaction. The sonication exfoliation process was then carried out for 30 min. A repeated washing process was carried out by centrifugation at 4000 rpm for 30 minutes until the residual liquid reached a pH of 7. Finally, the material was dried in an oven at 65 °C for 12 hours.

2.2. TiO_2/GO nanocomposites

2.2.1. Synthesis method by photo-sonification

The synthesized GO and the commercial anatase TiO_2 powder were separately suspended in a 30% ethanol aqueous solution and using an ultrasonic bath (*Branson 2510*) at a frequency of 40 *k*Hz for 15 minutes to obtain a homogeneous suspension.

978-1-6654-5508-4/22/$31.00 ©2022 IEEE

After 15 min, the GO suspension was poured into the TiO_2 suspension, continuing the ultrasound exposure until 40 minutes were reached. The sample was placed inside a photoreaction system under visible radiation from a 100 W metal halide lamp and continuous agitation for 24 hours. Finally, the resulting solution was dried on a heating plate at 80°C for 12 hours.

2.2.2. *Synthesis method by ball-milling*

Nanocomposites by ball-milling were prepared at room temperature. Commercial anatase TiO_2 and GO were mixed using a weight ratio of 98:2 and milled using a high-speed ball mill with 14 mm diameter silicon carbide balls at 300 rpm for 8 hours.

2.2.3. *Characterization*

A D2 PHASER Bruker diffractometer was used for XRD analysis under Cu-Kα radiation (λ=*1.54056 Å*) using a voltage of 40 kV and a current of 30 mA. The scanning range for the GOs was performed at 2θ from 8°-40°, while the nanocomposites were analyzed at 2θ from 10°-60°, both with a scanning speed of 0.02°/min, additionally the Bragg equation (*equation 1*) [21] was applied to the reflection (001) to estimate the average d_{hkl} distance between graphene layers. Raman spectra measurements were performed with the NT-MDT Ntegra Spectra, using a green laser at 532 nm. Fourier transform infrared (FTIR) spectroscopy was performed on a Perkin-Elmer Frontier FTIR instrument, using a diamond ATR accessory in the range of 1000-3500 cm^{-1} with a resolution of 4 cm^{-1}. Elemental mappings of nanocomposites were performed with a Hitachi S5500 FESEM microscope at an acceleration voltage of 5 kV. The specific surface area of the nanocomposites was measured by 15-point nitrogen adsorption (Brunauer- Emmett-Teller (BET): Micromeritics, Gemini 3240) after degassing the powder at 150°C for 12 h in nitrogen.

$$2d_{hkl}\, sin\theta = n\lambda \qquad (Eq.\ 1)$$

2.2.4. *MB adsorption experiment*

The percentage removal of Methylene Blue (MB) from the nanocomposites prepared by each synthesis method was evaluated using a 1 g/L dose. 100 mL of a 10 ppm MB solution was treated. The MB dye solution and TiO_2/GO nanocomposites were subjected to vigorous stirring in the dark for 210 min. Samples were taken every 3 min, centrifuged immediately, and analyzed with a UV-Vis spectrophotometer (*JASCO spectrometer model V-670*) to estimate the concentration values of the MB dye solution. The maximum wavelength selected to measure the MB dye concentration was 663 nm using deionized water as a reference. The removal efficiency, R (%) were calculated by the following equations:

$$R\ (\%) = \left(\frac{C_0 - C_e}{C_0}\right) x\ 100 \qquad (Eq.\ 2)$$

Where, C_0 and C_e are initial and equilibrium concentrations of MB dye (mg/L), respectively.

3. Results and discussion

3.1. *Graphene oxide (GO)*

A comparison of the XRD spectra of the precursor graphite with the synthesized graphene oxide is shown in figure 1. A sharp signal is observed in the graphite at 2θ≈26.15°, corresponding to the (002) plane of the graphite [22], confirming the presence of a well-organized layered structure with an interplanar distance d_{hkl}≈0.34 nm. On the other hand, in the GO pattern, it is observed that the intensity of the (002) plane of graphite reduced its intensity considerably, and at the same time, a signal appears at 2θ≈11.84°, corresponding to the (001) plane of graphene oxide, being this an indicator of the oxidation of the material [23]. Furthermore, after calculating the interplanar distance using Bragg's law (d_{hkl}≈0.899 nm), an increase was found compared to that of the precursor graphite, attributing this to the intercalation of functional groups such as epoxy, hydroxyl, carbonyl, and carboxyl in the basal plane of the graphite [24].

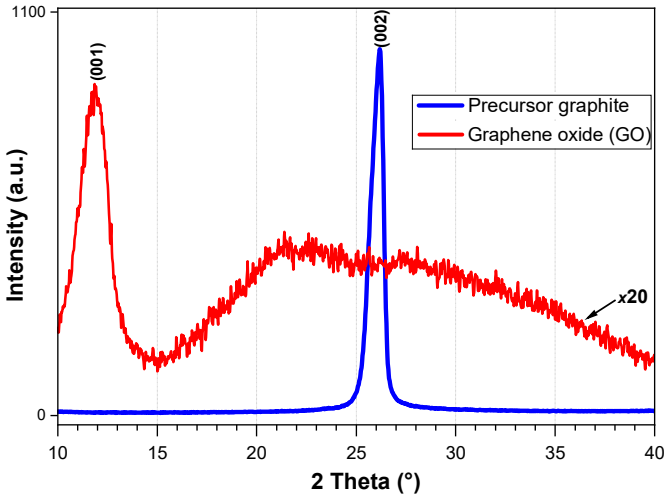

Figure 1. *XRD spectra of the precursor graphite and GO by Tour method*

Figure 2 shows a comparison of the Raman spectra of the precursor graphite and GO. In graphite, the presence of a strong G-band at ~1579 cm^{-1} attributed to C=C stretching and appearing in all sp^2 carbon structures is observed, while the D-band at ~1347 cm^{-1} is attributed to the presence of defects in the graphite material [25]. In GO, a shift of the G-band towards higher wavenumbers was observed, this being attributed to the formation of more sp^3 states in the lattice [26]. Likewise, changes were observed in the D band, since, because of the incorporation of more oxygenated groups, its intensity increased, and the signal broadened [27]. Using the intensities of the D and G bands, we calculated the I_D/I_G ratio, which indirectly indicates the average size of the aromatic group. As expected, and I_D/I_G ratio of GO>graphite was calculated, thus verifying the higher presence of sp^3 states because of defects

and disorder in the GO structure compared to the precursor graphite [28].

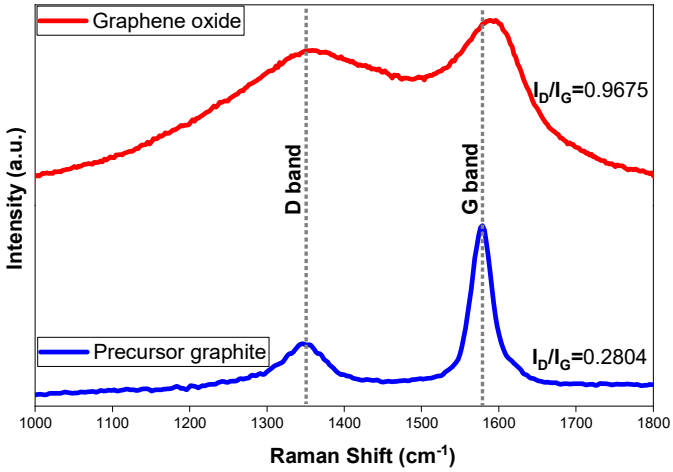

Figure 2. *Raman spectra of the precursor graphite and GO by Tour method*

Figure 3 shows the FT-IR spectra for the precursor graphite and the GO. No significant signals were observed in graphite, coinciding with previous reports reported in the literature [29-32]. While in GO, the signal corresponding to the presence of hydroxyl groups was observed at ~3302 cm^{-1} and stretching of water with hydrogen bonding (H-O-H) at ~3200 cm^{-1}. At ~1722 cm^{-1} the -C=O stretch corresponding to the carboxyl groups was found and the C-O-C stretch (epoxide group) appeared at two wavelengths (~1373 cm^{-1} and ~1200 cm^{-1}) [33]. Finally, the C=C bonds of the non-oxidized domains were observed at ~1556 cm^{-1} [34]. The presence of intensities corresponding to the functional groups, confirms the oxidation of graphite and the formation of GO [35], being complementary to the previous spectra by XRD and Raman, respectively.

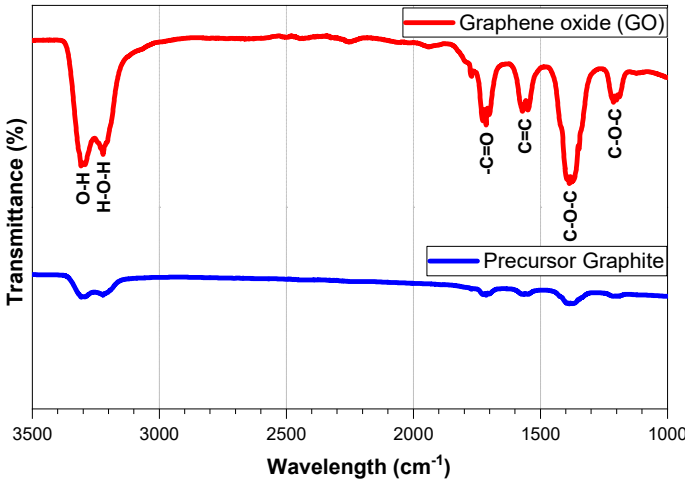

Figure 3. *FT-IR of the precursor graphite and GO by Tour method*

3.2. TiO_2 nanocomposites

Figure 4 shows the XRD patterns for commercial TiO_2 anatase used as precursor compared to TiO_2/GO nanocomposites obtained by photo-sonication and ball milling, respectively. In the commercial powder, the (101), (004), (200), (105), and (211) planes of the anatase phase (*JCPDS fiche n°. 21-1272*) are observed at 2θ ≈ 25.90, 37.68, 47.94°, 53.77°, 54.94°. These same planes, characteristic of the anatase phase, are observed in the diffractogram of the nanocomposite made by photo-sonication. While in the diffractogram corresponding to the nanocomposite obtained by ball-milling, a mixture of phases was found. Signals at 2θ ≈ 27.41°, 36.29°, 41.47°, and 43.57° were respectively attributed to the (110), (012), (111), and (210) planes of the rutile phase (*JCPDS fiche n°. 21-1276*). It is noted that not all the anatase phase was transformed into rutile because the diffraction signals of the anatase phase are still mostly present. The phase mixing in the nanocomposite by ball-milling was attributed to the chemical reactions within the atoms triggered by the increase of energy stored within the mixture [36], caused by the increase of temperature and local pressure at the collision sites of the powder and balls [37, 38], due to the ball-milling process. Both composites, photo-sonication, and ball-milling made, appear to have broader diffraction signals in comparison to the bare TiO_2. This is ascribed to a low crystallite size obtained because of the sonication and milling processes, respectively. Also, the effect is highly visible for the ball-milling sample, where the shape of the signals resembles a classic nanosized particle diffractogram. As well, a contraction of the TiO_2 lattice is revealed by a shift of its diffraction signals to higher angles; again, the effect is more evident in the ball-milled sample. This behavior is often related to the incorporation of GO into the TiO_2 matrix.

On the other hand, there is a lack of carbon signals in both nanocomposite spectra. This is attributed to a masking effect of the TiO_2 over the C signals, often explained by the diffusion of C atoms, which possess smaller atomic radii (0.0914 nm), into the Ti lattice (0.1448 nm) [39], being the elemental diffusion the mechanism of formation of the materials [40]. Further discussion on the presence of GO in both samples will be provided by the Raman analysis.

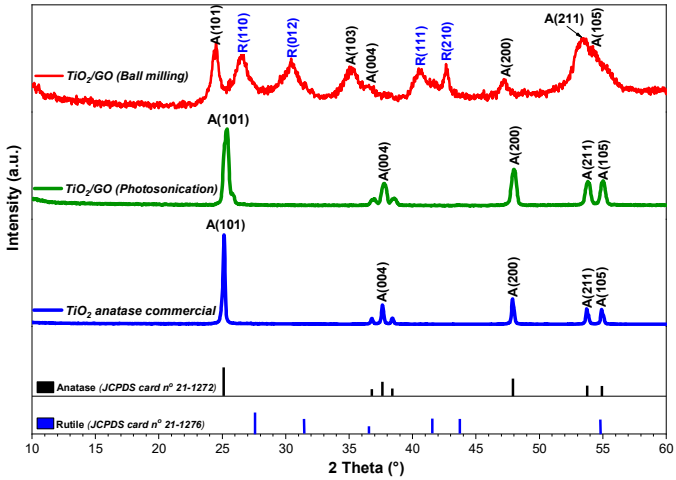

Figure 4. *XRD patterns of TiO_2/GO nanocomposites by photo-sonication and ball-milling compared to TiO_2 anatase commercial*

Figure 5 shows the Raman spectroscopy of the samples. In commercial anatase TiO_2, the presence of four characteristic vibrational modes of the anatase phase was confirmed at ~149.4, ~402.21, ~522.55, and ~645.02 cm^{-1} corresponding to E_g, B_{1g}, A_{1g}, and E_g symmetries, respectively [41]. So also, the same vibrational modes were observed in the photo-sonication nanocomposite. For the ball-milling nanocomposite, the presence of the anatase phase was verified with the E_g vibrational mode at 161.83 cm^{-1}, and additionally the E_g and A_{1g} modes of the Rutile phase at 427.37 and 617.43 cm^{-1}, respectively [42]. XRD and Raman analyses confirmed the formation of anatase and rutile phases of TiO_2 in the nanocomposite by ball milling, additionally, two bands were observed around ~1361.31 cm^{-1} (*D band*) and ~1609.23 cm^{-1} (*G band*) demonstrating the presence of graphene oxide in the composite. The presence of D and G bands in TiO_2/GO nanocomposites indicates a strong interaction between the individual materials (TiO_2 and GO), which means that they can work simultaneously on an application [43].

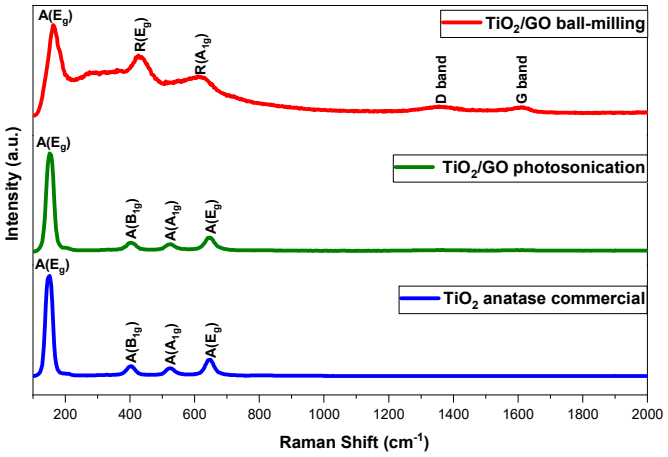

Figure 5. *Raman of TiO_2/GO nanocomposites by photo-sonication and ball-milling compared to TiO_2 anatase commercial*

Finally, figure 6 shows a comparison of elemental mappings of both nanocomposites. By ball milling a more homogeneous distribution of the C belonging to the GO is observed while by photo-sonication isolated regions are appreciated with carbon, demonstrating with it the better integration of both materials is carried out by ball milling.

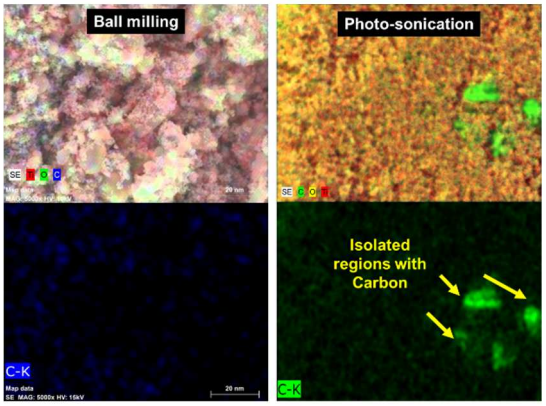

Figure 6. *Ball milling and photo-sonication elemental mappings*

3.3. MB adsorption of TiO_2/GO nanocomposites

Figure 7 shows the MB removal results of commercial TiO_2 compared to nanocomposites by ball-milling and photo-sonication, respectively. It was observed that, after 210 min, commercial TiO_2 alone achieved an adsorption removal of ~33.9%. Our results are comparable with those reported by Ertuş *et al*. 2021, who removed ~32.3% MB [44]. After the incorporation of GO into the TiO_2 matrix, we verified an improvement in the removal efficiency. The nanocomposite synthesized by photo-sonication after ~200 min showed removal of ~40.57%, this being an 8% improvement compared to the single material. Whereas, with the ball-milling synthesized nanocomposite, an improvement of more than 33.1% was found, with the removal of ~65.11%, after 200 minutes of exposure. This is attributed to a better and/or correct integration of the GO to the TiO_2 in the nanocomposite, being previously observed with the XRD and Raman spectra, where the results indicate a strong interaction between TiO_2 and GO phases; also, an inferred enhancement in the specific area of the milled sample play a beneficial role in the adsorption property. In both cases, minimal rises and falls were also observed, attributed to desorption before the material reached removal equilibrium. Such equilibrium was reached by ball-milling after 30 minutes, while by photo-sonication it was reached after 150 minutes of testing. In summary, the ball milling method was the most suitable for the manufacture of TiO_2/GO nanocomposites for application in MB dye removal by adsorption mechanism, due to the higher percentage of removal in less time.

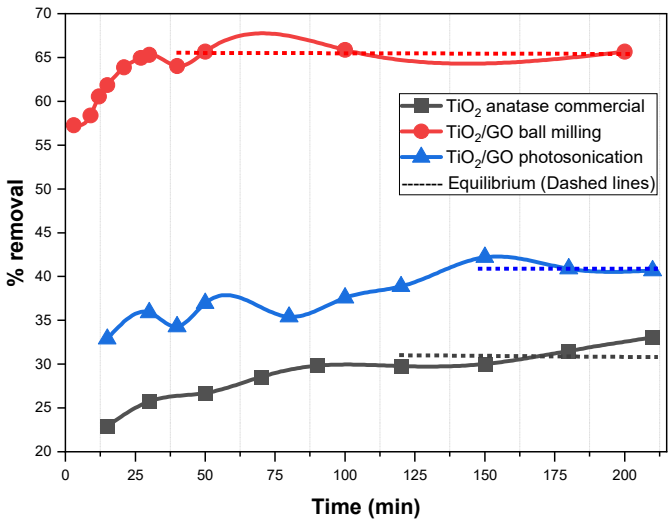

Figure 7. *MB removal percentage by commercial TiO_2 and TiO_2/GO nanocomposites by photo-sonication and ball milling.*

4. Conclusion

In this work, we synthesized GO by the Tour method and its incorporation into TiO_2 as nanocomposites using photo-sonication and ball-milling methods. After a comparison of the percentage of MB removal, we demonstrated that the incorporation of GO into the TiO_2 matrix improved the removal efficiency of the bare material. However, it was by the ball-

milling method that we achieved a ~65.11% removal of the dye, being this percentage better than that achieved with the nanocomposite by photo-sonication. Therefore, ball-milling allows us to create TiO_2/GO materials with good MB removal capacity by the adsorption mechanism and without using additional energy sources, not to mention that the adsorption equilibrium was reached much faster, thus representing a considerable reduction of the measurement time.

Acknowledgments

The authors acknowledge Ing. Miguel Ángel Avendaño Ibarra (Measurements by Raman spectroscopy), Ing. Miguel Ángel Luna Arias (Measurements by UV-Vis spectroscopy), and Ing. Álvaro Guzmán Campuzano (Technical support) from CINVESTAV-SEES department; F. J. Cano acknowledge BE-UP language & coaching school for English Language grand. The authors acknowledge CONACYT for the doctoral scholarship awarded to F. J. Cano and the postdoctoral scholarship to Odín Reyes Vallejo.

References

[1] Yamashita, H., & Li, H. (Eds.). (2016). Nanostructured photocatalysts. *Springer*. https://doi.org/10.1007/978-3-319-26079-2

[2] Anpo, M., & Takeuchi, M. (2003). The design and development of highly reactive titanium oxide photocatalysts operating under visible light irradiation. *Journal of catalysis*, 216(1-2), 505-516. https://doi.org/10.1016/S0021-9517(02)00104-5

[3] Choi, W., Termin, A., & Hoffmann, M. R. (2002). The role of metal ion dopants in quantum sized TiO_2: correlation between photoreactivity and charge carrier recombination dynamics. *The Journal of Physical Chemistry*, 98(51), 13669-13679. https://doi.org/10.1021/j100102a038

[4] Di Paola, A., Marci, G., Palmisano, L., Schiavello, M., Uosaki, K., Ikeda, S., & Ohtani, B. (2002). Preparation of polycrystalline TiO_2 photocatalysts impregnated with various transition metal ions: characterization and photocatalytic activity for the degradation of 4-nitrophenol. *The Journal of Physical Chemistry B*, 106(3), 637-645. https://doi.org/10.1021/jp0130741

[5] Asahi, R. Y. O. J. I., Morikawa, T. A. K. E. S. H. I., Ohwaki, T., Aoki, K., & Taga, Y. (2001). Visible-light photocatalysis in nitrogen-doped titanium oxides. *science*, 293(5528), 269-271. https://doi.org/10.1126/science.1061051

[6] Khedr, T. M., El-Sheikh, S. M., Hakki, A., Ismail, A. A., Badawy, W. A., & Bahnemann, D. W. (2017). Highly active non-metals doped mixed-phase TiO_2 for photocatalytic oxidation of ibuprofen under visible light. *Journal of Photochemistry and Photobiology A: Chemistry,* 346, 530-540. https://doi.org/10.1016/j.jphotochem.2017.07.004

[7] Cano F.J., Romero-Nuñez, A., Jantrania, A., Liu, H., Kassiba, A., & Velumani, S. (2021, November). Bandgap dependence on facet and size engineering of TiO_2: A DFT Study. In 2021 18th International Conference on Electrical Engineering, Computing Science and Automatic Control (CCE) (pp. 1-5). *IEEE*. https://doi.org/10.1109/CCE53527.2021.9632880

[8] Parnicka, P., Mazierski, P., Grzyb, T., Wei, Z., Kowalska, E., Ohtani, B., ... & Nadolna, J. (2017). Preparation and photocatalytic activity of Nd-modified TiO_2 photocatalysts: Insight into the excitation mechanism under visible light. *Journal of Catalysis*, 353, 211-222. https://doi.org/10.1016/j.jcat.2017.07.017

[9] Reszczyńska, J., Grzyb, T., Wei, Z., Klein, M., Kowalska, E., Ohtani, B., & Zaleska-Medynska, A. (2016). Photocatalytic activity and luminescence properties of RE^{3+}–TiO_2 nanocrystals prepared by sol-gel and hydrothermal methods. *Applied Catalysis B: Environmental,* 181, 825-837. https://doi.org/10.1016/j.apcatb.2015.09.001

[10] Zielińska-Jurek, A., Kowalska, E., Sobczak, J. W., Lisowski, W., Ohtani, B., & Zaleska, A. (2011). Preparation and characterization of monometallic (Au) and bimetallic (Ag/Au) modified titania photocatalysts activated by visible light. *Applied Catalysis B: Environmental, 101(3*-4), 504-514. https://doi.org/10.1016/j.apcatb.2010.10.022

[11] Babudurai, M., Nwakanma, O., Romero-Nuñez, A., Manisekaran, R., Subramaniam, V., Castaneda, H., & Jantrania, A. (2021). Mechanical activation of TiO_2/Fe_2O_3 nanocomposite for arsenic adsorption: Effect of ball-to-powder ratio and milling time. *Journal of Nanostructure in Chemistry*, 11(4), 619-632. https://doi.org/10.1007/s40097-021-00388-8

[12] Sampaio, M. J., Silva, C. G., Marques, R. R., Silva, A. M., & Faria, J. L. (2011). Carbon nanotube–TiO_2 thin films for photocatalytic applications. *Catalysis Today,* 161(1), 91-96. https://doi.org/10.1016/j.cattod.2010.11.081

[13] Wang, F., & Zhang, K. (2012). Physicochemical and photocatalytic activities of self-assembling TiO_2 nanoparticles on nanocarbon surface. *Current Applied Physics*, 12(1), 346-352. https://doi.org/10.1016/j.cap.2011.07.030

[14] Li, S., Pan, X., Wallis, L. K., Fan, Z., Chen, Z., & Diamond, S. A. (2014). Comparison of TiO_2 nanoparticle and graphene–TiO_2 nanoparticle composite phototoxicity to Daphnia magna and Oryzias latipes. *Chemosphere*, 112, 62-69. https://doi.org/10.1016/j.chemosphere.2014.03.058

[15] Yan, H., Tao, X., Yang, Z., Li, K., Yang, H., Li, A., & Cheng, R. (2014). Effects of the oxidation degree of graphene oxide on the adsorption of methylene blue. *Journal of hazardous materials,* 268, 191-198. https://doi.org/10.1016/j.jhazmat.2014.01.015

[16] Cigarroa-Mayorga, O. E. (2021). Tuning the size stability of $MnFe_2O_4$ nanoparticles: Controlling the morphology and tailoring of surface properties under the hydrothermal synthesis for functionalization with myricetin. *Ceramics International*, 47(22), 32397-32406. https://doi.org/10.1016/j.ceramint.2021.08.139

[17] Cano, F. J., Castilleja-Escobedo, O., Espinoza-Pérez, L. J., Reynosa-Martínez, C., & Lopez-Honorato, E. (2021). Effect of Deposition Conditions on Phase Content and Mechanical Properties of Yttria-Stabilized Zirconia Thin Films Deposited by Sol-Gel/Dip-Coating. *Journal of Nanomaterials*, 2021. https://doi.org/10.1155/2021/4449890

[18] Sanchez, M. F., Sanchez, T. G., Courel, M., Reyes-Vallejo, O., Sanchez, Y., Saucedo, E., & Sebastian, P. J. (2022). Effect of post-annealing thermal heating on Cu_2ZnSnS_4 solar cells processed by a sputtering technique. *Solar Energy*, *237*, 196-202. https://doi.org/10.1016/j.solener.2022.04.002

[19] Rojas-Chávez, H., Cigarroa-Mayorga, O. E., González-Domínguez, J. L., Cayetano-Castro, N., Tellez-Cruz, M. M., Andraca-Adame, J. A., & Mondragón-Sánchez, M. L. (2018). The early nucleation of a eutectic alloy during high-energy milling. *Materials Research Express*, *5*(7), 076514. https://doi.org/10.1088/2053-1591/aad02d

[20] Kotsyubynsky, V. O., Boychuk, V. M., Budzulyak, I. M., Rachiy, B. I., Zapukhlyak, R. I., Hodlevska, M. A., ... & Bilogubka, O. R. (2021). Structural properties of graphene oxide materials synthesized accordingly to hummers, tour and modified methods: XRD and Raman study. *Physics and Chemistry of Solid State*, 22(1), 31-38. https://doi.org/10.15330/pcss.22.1.31-38

[21] Elton, L. R. B., & Jackson, D. F. (1966). X-ray diffraction and the Bragg law. *American Journal of Physics,* 34(11), 1036-1038. https://doi.org/10.1119/1.1972439

[22] Zeng, F., Sun, Z., Sang, X., Diamond, D., Lau, K. T., Liu, X., & Su, D. S. (2011). In situ one-step electrochemical preparation of graphene oxide nanosheet-modified electrodes for biosensors. *ChemSusChem*, 4(11), 1587-1591. https://doi.org/10.1002/cssc.201100319

[23] Titelman, G. I., Gelman, V., Bron, S., Khalfin, R. L., Cohen, Y. B. P. H., & Bianco-Peled, H. (2005). Characteristics and microstructure of aqueous colloidal dispersions of graphite oxide. *Carbon*, 43(3), 641-649. https://doi.org/10.1016/j.carbon.2004.10.035

[24] Karbak, M., Boujibar, O., Lahmar, S., Autret-Lambert, C., Chafik, T., & Ghamouss, F. (2022). Chemical Production of Graphene Oxide with High Surface Energy for Supercapacitor Applications. C, 8(2), 27. https://doi.org/10.3390/c8020027

[25] Dresselhaus, M. S., Jorio, A., Hofmann, M., Dresselhaus, G., & Saito, R. (2010). Perspectives on carbon nanotubes and graphene Raman spectroscopy. *Nano letters*, 10(3), 751-758. https://doi.org/10.1021/nl904286r

[26] Scardaci, V., & Compagnini, G. (2021). Raman spectroscopy investigation of graphene oxide reduction by laser scribing. *C*, 7(2), 48. https://doi.org/10.3390/c7020048

[27] Tuinstra, F., & Koenig, J. L. (1970). Raman spectrum of graphite. *The Journal of chemical physics,* 53(3), 1126-1130. https://doi.org/10.1063/1.1674108
[28] Compton, O. C., & Nguyen, S. T. (2010). Graphene oxide, highly reduced graphene oxide, and graphene: versatile building blocks for carbon-based materials. *small*, 6(6), 711-723. https://doi.org/10.1002/smll.200901934
[29] Khenfouch, M., & Ba, M. (2012). Morphological, vibrational and thermal properties of confined graphene nanosheets in an individual polymeric nanochannel by electrospinning. http://dx.doi.org/10.4236/graphene.2012.12002
[30] Manoratne, C. H., Rosa, S., & Kottegoda, I. R. M. (2017). XRD-HTA, UV visible, FTIR and SEM interpretation of reduced graphene oxide synthesized from high purity vein graphite. *Mater. Sci. Res. India*, 14(1), 19-30. http://dx.doi.org/10.13005/msri/140104
[31] Choi, E. Y., Han, T. H., Hong, J., Kim, J. E., Lee, S. H., Kim, H. W., & Kim, S. O. (2010). Noncovalent functionalization of graphene with end-functional polymers. Journal of *Materials Chemistry*, 20(10), 1907-1912. https://doi.org/10.1039/B919074K
[32] Hidayah, N. M. S., Liu, W. W., Lai, C. W., Noriman, N. Z., Khe, C. S., Hashim, U., & Lee, H. C. (2017, October). Comparison on graphite, graphene oxide and reduced graphene oxide: Synthesis and characterization. *In AIP Conference Proceedings* (Vol. 1892, No. 1, p. 150002). AIP Publishing LLC. https://doi.org/10.1063/1.5005764
[33] Zhao, G., Li, J., Ren, X., Chen, C., & Wang, X. (2011). Few-layered graphene oxide nanosheets as superior sorbents for heavy metal ion pollution management. *Environmental science & technology,* 45(24), 10454-10462. https://doi.org/10.1021/es203439v
[34] Guo, H. L., Wang, X. F., Qian, Q. Y., Wang, F. B., & Xia, X. H. (2009). A green approach to the synthesis of graphene nanosheets. *ACS nano*, *3*(9), 2653-2659. https://doi.org/10.1021/nn900227d
[35] Dresselhaus, M. S., Jorio, A., Hofmann, M., Dresselhaus, G., & Saito, R. (2010). Perspectives on carbon nanotubes and graphene Raman spectroscopy. *Nano letters*, 10(3), 751-758. https://doi.org/10.1021/nl904286r
[36] Quan, Y. U. A. N., Zheng, Y., & Yu, H. Z. (2011). Rapid synthesis of Ti (C, N) powders by mechanical alloying and subsequent arc discharging. *Transactions of Nonferrous Metals Society of China*, 21(7), 1545-1549. https://doi.org/10.1016/S1003-6326(11)60894-7
[37] Kim, B. R., Yun, K. S., Jung, H. J., Myung, S. T., Jung, S. C., Kang, W., & Kim, S. J. (2013). Electrochemical properties of the TiO_2 (B) powders ball mill treated for lithium-ion battery application. *Chemistry Central Journal,* 7(1), 1-5. https://doi.org/10.1186/1752-153X-7-174
[38] Rojas-Blanco, L., Espinoza-Beltrán, F. J., Mani-González, P. G., Ramirez-Bon, R., Zambrano, G., & Velásquez-Salazar, J. (2011). Photocatalytic activity in the visible region of high energy milled TiO_2:N nanopowders. *Revista Mexicana de Física, 57*(2), 36-40.
[39] Rajabi, A., & Ghazali, M. J. (2017). Quantitative analyses of TiC nanopowders via mechanical alloying method. *Ceramics International*, 43(16), 14233-14243. https://doi.org/10.1016/j.ceramint.2017.07.171
[40] Saba, F., Kabiri, E., Khaki, J. V., & Sabzevar, M. H. (2016). Fabrication of nanocrystalline TiC coating on AISI D2 steel substrate via high-energy mechanical alloying of Ti and C. *Powder Technology*, 288, 76-86. https://doi.org/10.1016/j.powtec.2015.10.030
[41] Su, W., Zhang, J., Feng, Z., Chen, T., Ying, P., & Li, C. (2008). Surface phases of TiO_2 nanoparticles studied by UV Raman spectroscopy and FT-IR spectroscopy. *The Journal of Physical Chemistry C*, *112*(20), 7710-7716. https://doi.org/10.1021/jp7118422
[42] Tamilselvan, V., Yuvaraj, D., Kumar, R. R., & Rao, K. N. (2012). Growth of rutile TiO_2 nanorods on TiO_2 seed layer deposited by electron beam evaporation. *Applied Surface Science*, *258*(10), 4283-4287. https://doi.org/10.1016/j.apsusc.2011.12.079
[43] Liu, L., Zhang, Y., Zhang, B., & Feng, Y. (2017). A detailed investigation of the performance of dye-sensitized solar cells based on reduced graphene oxide-doped TiO_2 photoanode. *Journal of Materials Science*, *52*(13), 8070-8083. https://doi.org/10.1007/s10853-017-1014-9
[44] Ertuş, E. B., Vakifahmetoglu, C., & Öztürk, A. (2021). Enhanced methylene blue removal efficiency of TiO_2 embedded porous glass. *Journal of the European Ceramic Society*, 41(2), 1530-1536. https://doi.org/10.1016/j.jeurceramsoc.2020.09.047